Accepted manuscript

Monitoring the fracture process of concrete during splitting using integrated ultrasonic coda wave interferometry, digital image correlation and X-ray micro-computed tomography
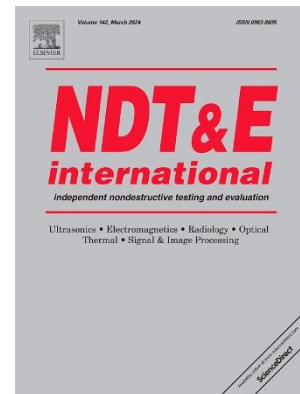
Erwin Wojtczak, Magdalena Rucka, Łukasz Skarżyński

In: *NDT & E International* 126, 102591

DOI: https://doi.org/10.1016/j.ndteint.2021.102591

Please cite this article as:

E. Wojtczak, M. Rucka, Ł. Skarżyński, Monitoring the fracture process of concrete during splitting using integrated ultrasonic coda wave interferometry, digital image correlation and X-ray micro-computed tomography, *NDT & E International* 126 (2022), 102591, doi: https://doi.org/10.1016/j.ndteint.2021.102591

Monitoring the fracture process of concrete during splitting using integrated ultrasonic coda wave interferometry, digital image correlation and X-ray micro-computed tomography

Erwin Wojtczak[1]*, Magdalena Rucka[1], and Łukasz Skarżyński[2]

1 Department of Mechanics of Materials and Structures, Faculty of Civil and Environmental Engineering, Gdańsk University of Technology, Narutowicza 11/12, 80-233, Gdańsk, Poland,

2 Department of Buildings Structures and Material Engineering, Faculty of Civil and Environmental Engineering, Gdańsk University of Technology, Narutowicza 11/12, 80-233, Gdańsk, Poland,

emails: erwin.wojtczak@pg.edu.pl, magdalena.rucka@pg.edu.pl, lukasz.skarzynski@pg.edu.pl

* corresponding author

Abstract

The paper deals with the continuous-time monitoring of mechanical degradation in concrete cubes under splitting. A series of experiments performed with integrated coda wave interferometry (CWI) and digital image correlation (DIC), supported with X-ray micro-computed tomography (micro-CT) is reported. DIC and micro-CT techniques were used to characterize the fracture process in detail. CWI method was proved to be effective in the assessment of damage level based on the changes in decorrelation between coda wave signals. The possibility of early detection of damage using CWI is promising for possible applications in the diagnostics of concrete elements.

Keywords

fracture monitoring; non-destructive testing (NDT); ultrasonic coda waves; digital image correlation (DIC); X-ray micro-computed tomography

1. Introduction

Concrete is considered to be one of the most popular building materials. Thanks to its advantages, e.g., high strength, durability and relatively low cost, it has found many applications in civil engineering. During the operation period, concrete elements may be subjected to various loads, among which the most dangerous for their safety are live loads and accidental effects. Design mistakes or uncontrolled increase in load value can lead to the initiation of fracture, which in turn lead to catastrophic consequences. Taking into account that concrete elements under load experience cracking, the observation of micro-crack occurrence before rupture is desired to give appropriate information. Since the destruction of concrete elements may have a sudden character, it is beneficial to characterize the fracture process and determine some indicators which could be used in early damage detection. It is important not

2

only for plain concrete but also (if not even more) for reinforced concrete elements, because open cracks may decrease the durability of the material by enabling the corrosion of steel.

Non-destructive testing (NDT) is an intensively developing trend in the diagnostics of materials and structures that is of increasing interest to many researchers. Among many methods, a few techniques can be favoured for concrete structures. X-ray micro-computed tomography (micro-CT) is a non-destructive method with many successful applications in the investigation of fracture process, enabling the visualization of the internal structure of concrete members, including, e.g., aggregates, pores, and reinforcement location or crack propagation paths [1–5]. Digital image correlation (DIC) is a powerful optical approach allowing imaging of local strain and displacement changes based on the comparison between photographs of the specimens collected during experimental investigations, e.g., under external load [6–12]. Significant development is also observed nowadays in the group of diagnostic techniques based on the phenomenon of elastic wave propagation including acoustic emission (AE) [13–15] and ultrasonic waves (UW) [16–20].

A promising approach is based on the analysis of diffuse waves, also known as coda waves. The term 'coda' was adopted from seismology, where it refers to the tail of seismograms representing ground motion during earthquakes [21,22]. Diffuse waves are a specific kind of guided waves that appear as an effect of multi-scattering of elastic waves in heterogeneous media [23] with high sensitivity to any disturbances occurring in the structure. Coda wave interferometry (CWI) is a powerful technique based on diffuse wave presence, with many applications in the monitoring of temperature changes [24–26] or stress state [27,28]. Some successful applications have been also reported in the case of non-destructive damage detection. Chen et al. [29] used ultrasonic coda waves to monitor contamination cleaning. The simple decorrelation coefficient was applied to observe changes in the cleaning of wax deposits on the surface of stainless steel ducts. In [30], Sang et al. considered the application of CWI for the analysis of the evolution of fatigue-induced damage in shale cylinders under cyclic compression tests until failure. Cross-correlation was used to determine the time shift and time stretching between signals in the intact and loaded state. Hafidi et al. [31] used diffusive waves for damage detection in a periodic medium consisting of steel rods immersed in water. They proposed experimental-theoretical approaches for topological imaging of the defect in the form of a missing rod. Taking into account the complex structure of composites, they achieved great interest of researchers dealing with diffuse waves. Pomarède et al. [32] applied CWI for the monitoring of micro-cracks in woven CFRP composite. They analysed the relative velocity changes and variation of decorrelation between signals in the reference and damaged state

3

during quasi-static bending tests. In their work [33], Zhu et al. considered delamination detection in a unidirectional CFRP plate under bending. They applied cross-correlation in its stretching variant, i.e., they searched for the optimal time-stretching factor that provides the best correlation of signals in reference and damage states. So-called Locadiff approach using damage sensitivity kernel was used for damage imaging. Gao et al. [34] used coda waves for disbond detection in an aeronautical honeycomb composite sandwich. They applied windowed cross-correlation for the determination of the time delay evoked by disbond presence. A quantitative damage assessment was provided by the energy index, defined as a ratio of local power spectrum density calculated for damaged and intact states. Spytek et al. [23] considered damage imaging in aluminium and CFRP plates using ultrasonic coda waves. They used synthetic time-reversal of diffuse Lamb waves for the mean wavenumber estimation algorithm.

Being a complex and highly heterogeneous material, concrete has appeared as an object of coda wave-based non-destructive diagnostics in some previous studies. Schurr et al. [35] used CWI for non-destructive detection of damage in concrete prisms under compression cyclic load and temperature changes. They used a cross-correlation approach to determine the relative velocity changes of ultrasonic waves. In work [36] Schurr et al. used the CWI technique for early-stage damage detection in concrete under mechanical degradation (dynamic compressive load and chemical reaction). The authors correlated stresses with relative velocity changes obtained from the stretching approach. Shokouhi [37] analysed concrete prisms under uniaxial compression applied in loading-unloading cycles. The relative velocity changes determined using the CWI technique and time of flight calculation were compared to the stress state. Planès and Larose [22] presented a comprehensive review of the application of ultrasonic CWI for the non-destructive assessment of concrete elements. They reported successful applications of cross-correlation of coda waves in the monitoring of thermal changes, acousto-elasticity, stress variations, and damage monitoring. Planès et al. [38] presented a study on the theoretical prediction of decorrelation and phase-shift of coda waves caused by local changes in the case of multiple scattering medium. Some analytical expressions of the decorrelation and time-shift were related to the sensitivity kernel. Numerical simulations were performed to validate the theoretical estimation. In paper [39] Planès et al. considered imaging of local changes based on numerical simulations of wave propagation in heterogeneous media. The inverse method was introduced to visualize structural changes corresponding to the presence of additional scatterers in the analysed medium. Hillouin et al. [40] considered the detection of small cracks in mortar cementitious samples under bending forces by implementing CWI and nonlinear acoustic modulation using high-frequency signals (200-800 kHz) and pump waves (10-50 kHz). They

4

observed wave velocity changes by calculating the decorrelation of coda waves. Liu et al. [41] proposed using Taylor series expansion as a low-time consuming alternative for cross-correlation calculations to analyse relative velocity changes in concrete cylinders under compression. Larose et al. [42] applied coda waves and Locadiff technique to detect and locate pre-existing cracks and analyse the development of damage at the track tip in concrete prism under the four-point bending test. The so-called inversion procedure was used to prepare three-dimensional maps of density of mechanical changes allowing to visualize the damage. Zhang et al. [43] also used diffuse waves and Locadiff technique but to localize and image cracks on a prestressed concrete wall of an aeronautical wind tunnel. Fröjd and Ulriksen [44] analysed the efficiency of different frequencies of ultrasonic waves on the efficiency of CWI. They detected boreholes in large-scale concrete floor slabs under bending and concluded that higher frequencies (above 50 kHz) are efficient for this type of structure due to the high ability to create diffuse waves. Xie et al. [45] simulated coda wave propagation using the 2D finite-difference time-domain method to validate the assumption that total decorrelation occurring in a particular medium is the sum of decorrelations induced by all particular changes. The Locadiff technique was used to characterize extended changes located at various positions of the medium. Hafiz and Schumacher [46] used diffuse waves for monitoring of stresses in concrete elements (cylinders, prisms and real-scale bridge girder and column). The changes in applied stress were correlated to the changes in ultrasonic waveforms obtained using mangnitude-squared coherence estimation. Spalvier et al. [47] analysed the issue of monitoring stress changes in concrete pillars using cross correlation of coda waves. Four different metrics were compared, i.e., signal energy, cross correlation amplitude, cross correlation time and cross correlation symmetry. Hu et al. [48] proposed a novel stretching factor accumulation method for CWI to calculate relative velocity changes. They analysed concrete cubes under compression with loading-unloading steps such as relaxation and load fixing periods.

The latest trend in the diagnostics of concrete elements, reflected in a number of scientific works, is an integrated application of more than one NDT technique. Rouchier et al. [49] considered damage monitoring in fibre-reinforced mortar prisms under tensile load. They used DIC for imaging of micro- and macro-cracks and AE to localize and quantify damage. In [50], Zhang et al. also considered an application of DIC and AE on large-scale concrete bridge girders. DIC was proved to be efficient in crack evaluation, however, AE turned out more efficient in early detection of damage state. Skarżyński [51] used DIC and micro-CT to evaluate mechanical and radiation shielding properties of boron-basalt fibre-reinforced concrete prisms. Skarżyński and Marzec [52] applied DIC to characterize the shear fracture of concrete beams

5

reinforced with steel and basalt bars. Micro-CT was also used to perform numerical simulations of sample behaviour, taking into consideration the exact microstructure of concrete. Rucka et al. [53] analysed the fracture process of polyolefin fibre-reinforced concrete beams. Particular wave characteristics, i.e., changes of magnitude and phase, were assessed as efficient damage indicators thanks to the simultaneous application of DIC and UW techniques. It is, however, important to note, that synchronized use of CWI, DIC and micro-CT was not considered for early detection of fracture in concrete elements under splitting.

The main contribution of the current paper is a study on the integrated application of different diagnostic methods for monitoring fracture in concrete prisms under splitting. The novelty of the work concerns the continuous-time monitoring of 2D and 3D mechanical degradation in concrete utilizing the integrated DIC and CWI techniques supported with micro-CT scanning. The results of DIC revealed the moment of induction of fracture process zones and provided detailed imaging of cracks on the 2D surface of analysed concrete samples. DIC also allowed determining the moment of macro-crack initiation thanks to the support of continuous wavelet transform (CWT). Micro-CT scans allowed tracing crack paths inside specimens. Based on the processing of signals of ultrasonic coda waves with CWI, overall information about the state of samples in 3D was given. A detailed characterization of particular stages of the fracture process (intact state, micro-crack initiation and coalescence, stable micro-crack propagation, and macro-crack propagation) was conducted by the establishment of thresholds on decorrelation functions between consecutive ultrasonic coda wave signals. Additionally, analysis of decorrelation between frequency spectra of the signals was proposed and proved to be even more efficient than comparing time histories of coda waves. The comparison between the measurement methods allowed developing a non-destructive approach for early damage detection and monitoring with CWI as an autonomous technique with promising practical applications. The ability of each method for the analysis of the evolution of fracture process zones (FPZs) was carefully investigated. The opportunities and limitations of proposed techniques were characterized.

2. Materials and Methods

2.1. Specimens

The experimental research was performed on four concrete cubes with dimensions of $7 \times 7 \times 7$ cm^3. The size of the specimens has been selected in order to be entirely visible in the field of view of the X-ray micro-CT system (described below). The specimens were cut out from a single concrete prism of dimensions $10 \times 10 \times 50$ cm^3 in such a way that the cut covered

each surface. The ingredients of concrete were: cement type CEM I 42.5R (330 kg/m^3), water (165 kg/m^3), aggregate 0/2 mm (710 kg/m^3), aggregate 2/8 mm (664 kg/m^3), aggregate 8/16 mm (500 kg/m^3), and super-plasticizer (0.7% of cement content). The global dimension of the specimen was about 4.4 times the size of the greatest aggregate. The slump test performed on fresh mix resulted in the slump equal to approximately 140 – 145 mm, thus the consistency class was S3. The compression strength of the material was examined after 28 days of curing on three additional cubic prisms with the dimensions of 15 × 15 ×15 cm^3. The mean strength was equal to 52.73 MPa with a standard deviation of 3.47 MPa, thus the strength class was established as C40/50. A single notch with a width of 5 mm and a depth of 15 mm was cut in the middle of the specimens to induce the splitting failure. Additionally, the front surface of the specimens was covered by a random pattern for DIC measurements.

2.2. Experimental setup

The wedge splitting test (WST) was carried out on four concrete samples, denoted as specimens #1 to #4. The cubes were supported on the linear steel bar in the lower part and subjected to splitting in Zwick/Roell Z10 universal testing machine (UTM) with the use of a steel wedge in the upper part. A preload of 20 N was applied, after which the process of splitting was conducted with a constant displacement rate of 0.1 mm/min. The tests were stopped after 900 s, which corresponds to the displacement of 1.5 mm.

To characterize the fracture process, integrated UW and DIC methods were applied during quasi-static splitting tests. DIC technique was chosen based on its high efficiency in visual and quantitative describing fracture process on the 2D sample surface. Simultaneously, ultrasonic waves are able to propagate through the sample in 3D, thus they allow observing about fracture inside the sample, but do not provide such detailed information as DIC. Figure 1 shows the experimental setup, instrumentation, and sample under testing. Ultrasonic waves were excited and registered with an interval of 2 s, by means of three multilayer piezoelectric transducers NAC2024 manufactured by Noliac. One of them acted as an actuator (A), while the other two operated as sensors (S1, S2). The actuator was bonded on the left surface of the specimen. Sensor S1 was located at a distance of 8 mm from the actuator, while sensor S2 was located opposite to sensor S1, on the right surface of the specimen. The excitation was a wave packet composed of 5-cycle sine wave modulated by the Hann window. The frequency of the wave was 500 kHz. The excitation signal was generated by an arbitrary waveform generator AFG3022C and amplified by a high voltage amplifier AB A400DI. Wave propagation signals of a length of 5 ms were collected by a digital oscilloscope PicoScope 4824 with a sampling

7

frequency of 8 MHz. At the same time, photographs of the front surface of the cubes were taken every 2 s by ARAMIS MC 2D 12M system to observe the change of strain and crack evolution. The camera resolution was 4096 × 3000 pixels. Collected images were processed with Aramis Professional software. The assumed region of interest covering the front surface of the cube was divided into facets of a size of 19 × 19 pixels with a distance of 16 pixels. All experimental data used in this paper is available at [54–57].
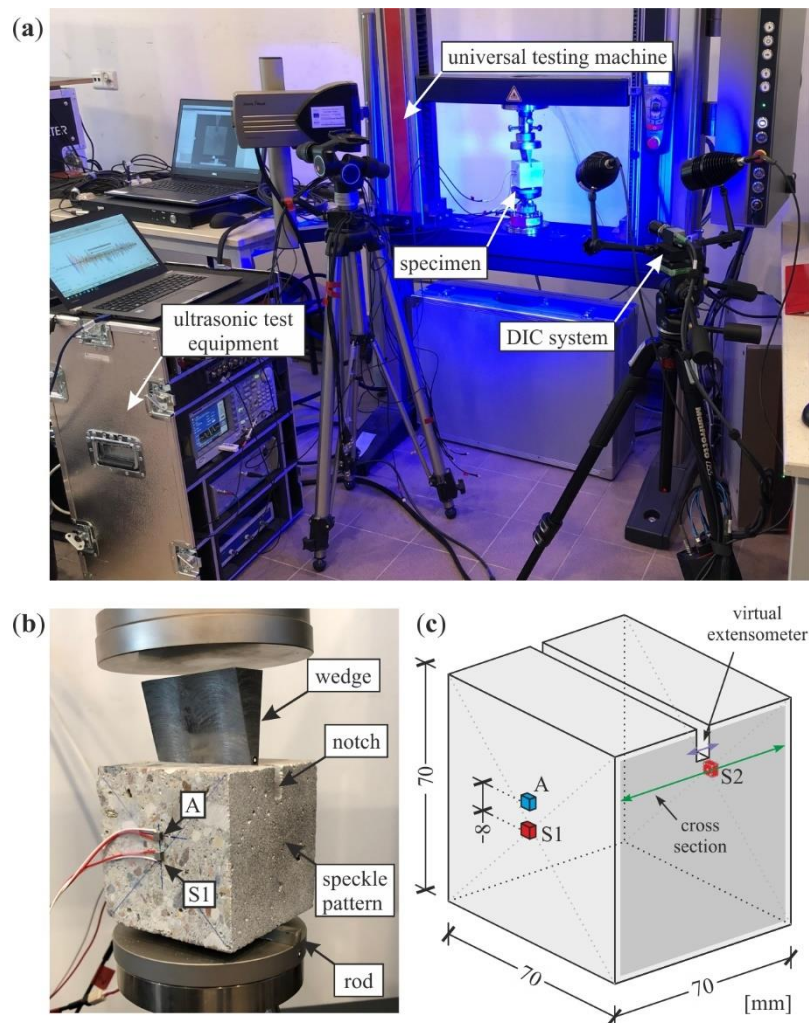

Figure 1. Experimental setup: instrumentation for wedge splitting test, ultrasonic testing, and digital image correlation(**a**); specimen under wedge splitting test (**b**); and location of piezoelectric transducers (**c**)

2.3. X-Ray Micro Computed Tomography

To characterize the material microstructure of the tested concrete samples, the technique of X-ray micro-computed tomography was used (see Figure 2). Specimens #1 to #4 were tested employing the SkyScan 1173 micro-CT scanner. The scans were carried out after conducting the splitting tests to image the 3D internal structure of the cubes (i.e., shape, size, and distribution of the aggregate and air voids) and to visualize the cracks inside the material. The following parameters were used during measurements: brass filter, an X-ray source voltage of

8

130 keV, a current of 61 μA and an exposure time of 4000 ms. Scan rotation was 180° with a rotation step of 0.3° and the size of the voxel of the μCT image was 39.68 μm. After μCT scanning, the reconstruction of the images was performed. The scanning time was about 3 h. The image reconstruction was carried out with the NRecon software. To choose the reconstruction parameters (post-alignment, beam-hardening correction, ring artefact correction and smoothing level), a fine-tuning method was used (one parameter was adjusted while keeping all other parameters fixed). The aim was to obtain a sharp image with different phases clearly distinguished. The post-alignment option (using 8 pixels) compensated for a small misalignment of the scanned object. The fifth-order polynomial function was used for a beam-hardening correction. The pixel smoothing (a region of 5 pixels) was applied to the projection in the form of a Gaussian function. After reconstruction, the images were analysed with the DataViewer and CTAn software. Despeckle and bitwise operations were carried out to improve image quality.
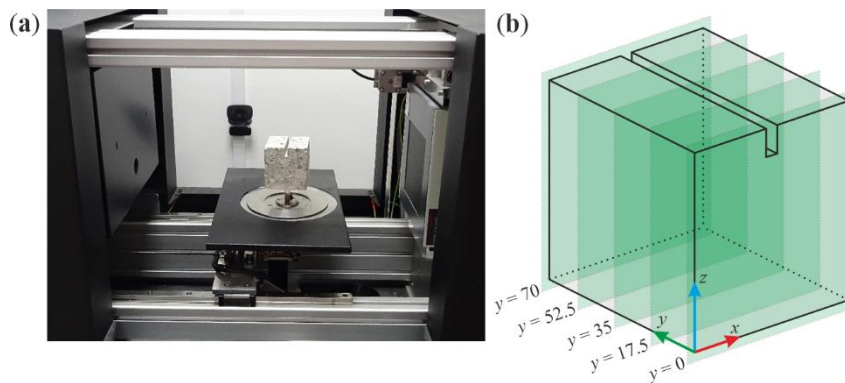

Figure 2. Micro-CT scanning: concrete sample placed on the rotation table of micro-CT 1173 Skyscan testing station (**a**); view of particular vertical cross-sections (**b**)

2.4. Coda Wave Interferometry for degradation monitoring

In the case of highly heterogeneous media, e.g., concrete, ultrasonic waves propagating through the examined element experience intensified scattering at the inhomogeneities (like aggregates with different sizes and locations), generating slowly decaying waves, namely coda waves or diffuse waves. In the current study, the wavelength is equal to 9.4 mm, thus the characteristic dimension of the cube (70 mm) is about 7.5 times the wavelength. Assuming that the heterogeneties are mostly gravel grains with the size above 8 mm, the wavelength satisfies the condition of multiple scattering regime [22], in which coda waves occur. Coda Wave Interferometry (CWI) technique is an ultrasound-based method with high efficiency in the detection of degradation state of heterogeneous materials. Despite their noisiness and disorderliness, coda waves are characterized by high repeatability if no changes of the actual state of the medium occur [31]. If any, even a small change in position of the inhomogeneities (acting like scatterers) occurs, e.g., when structural discontinuities (like micro- or macro-

cracks) appear, the wave scattering is affected, thus a change is observed in coda waves. This fact constitutes the basis for CWI, thus the method consists in the comparison between the ultrasonic signals collected in a reference (generally, intact) state and a damaged one. It is, however, essential to note that the presence of coda waves is not equally observed in the whole signal. Figure 3 shows the comparison of two representative waveforms collected in intact and damaged states for the same object. The time-domain can be divided into three noteworthy ranges. The first is a direct wave range in which no substantial changes between signals are observed. The second one is the coda wave range, where the differences are evident, thus this part of the signal is important for the diagnostics. The last piece, when the amplitude of propagating waves vanishes, is the noisy range. It is noteworthy that only short-time waveforms from each range are presented in the figure because the limits between the parts could not be clearly determined without detailed analysis. Therefore, for efficient results, it is important to appropriately choose the part of the signal covering only the coda wave range and neither the direct wave nor the noisy range.
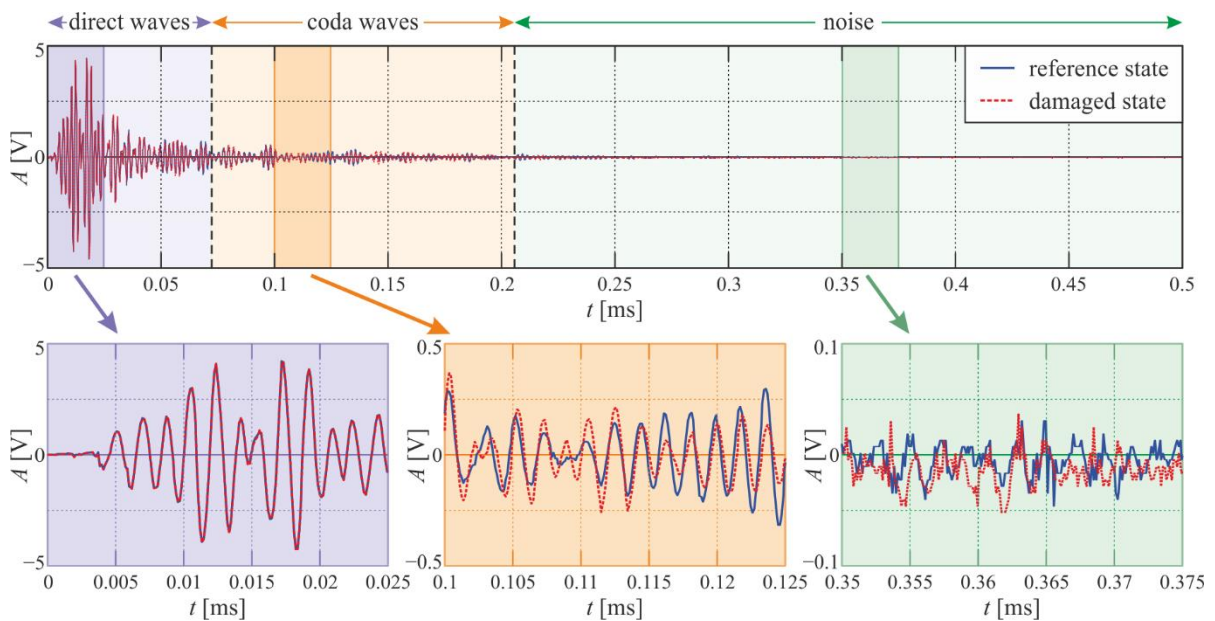

Figure 3. Comparison of signals of ultrasonic waves propagating in intact (reference) and damaged states with close-ups of the representative parts of the characteristic signal ranges.

The difference between the reference signal $s_r(t)$ and another particular signal during degradation $s_n(t)$ can be quantitatively measured by calculating the so-called decorrelation coefficient (DC)

$$DC^{(s)} = 1 - \frac{\int_{t_1}^{t_2} s_r(t) \cdot s_n(t) \, \mathrm{d}t}{\sqrt{\int_{t_1}^{t_2} s_r^2(t) \, \mathrm{d}t \cdot \int_{t_1}^{t_2} s_n^2(t) \, \mathrm{d}t}}. \tag{1}$$

10

In the formula, t_1 and t_2 denote the start and end time instances, respectively. The DC gives information about the appearing differences between signals. It is important to note that changes can be also observed in the frequency domain by calculating the decorrelation between the frequency spectra of signals obtained by the fast Fourier transform (FFT) of coda waves. For this purpose, the Fourier coefficients $X(\omega)$ are determined for each time-domain signal $s(t)$ using the following formula

$$X\left(\omega\right) = \int\limits_{-\infty}^{\infty} s(t)e^{-i\omega t}\mathrm{d}t \,. \tag{2}$$

The Fourier coefficients can be easily represented in relation to frequency f instead of the circular frequency ω. Decorrelation coefficient can be further calculated between the reference spectrum $X_r(f)$ calculated for the first signal and any consecutive spectrum $X_n(f)$ obtained for another signal in the frequency range between f_1 and f_2, covering non-zero frequency components. The Eq. (1) can be then rewritten in the following form

$$DC^{(f)} = 1 - \frac{\int\limits_{f_1}^{f_2} X_r(f) \cdot X_n(f)\mathrm{d}f}{\sqrt{\int\limits_{f_1}^{f_2} X_r^2(f)\mathrm{d}f \cdot \int\limits_{f_1}^{f_2} X_n^2(f)\mathrm{d}f}} \,. \tag{3}$$

3. Results and Discussion

3.1. Quasi-static split test

The results of the quasi-static splitting test are given in Figure 4. The peak load values (global maxima) for all cubes #1 – #4 are: 4.35 kN, 4.94 kN, 6.12 kN and 5.33 kN, consecutively. The mean value is 5.18 kN, the standard deviation (STD) is 0.74 kN, thus the coefficient of variation (COV) equals 14%, which could be assumed acceptable for concrete elements. Figure 4 shows load-CMOD curves determined based on the results from the virtual extensometer (obtained from DIC measurements, see Figure 1c), i.e. measurements of displacement evolution between two assumed points. The repeatability of the results is clearly visible – similar stiffness in the pre-peak regime and rate of softening in the post-peak regime could be observed.
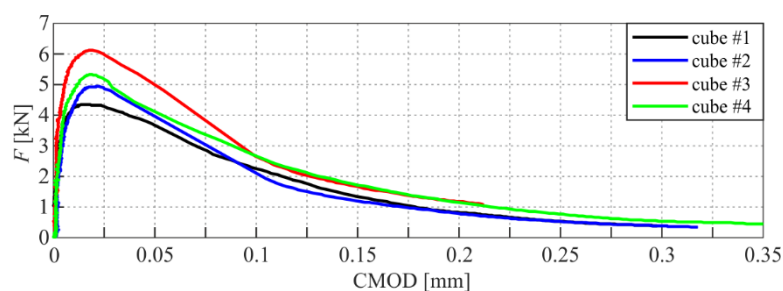

Figure 4. Load-CMOD curves for cubes #1 – #4

3.2. Digital Image Correlation

The evolution of fracture process zones (FPZs), corresponding to the regions with intensified strain values, was visualised based on the photographs taken during the experiments using DIC technique. Figure 5 shows the major strain fields for all cubes at different time instances determined based on the percentage of peak F_{max} (see Figure 4). To obtain optimal imaging, the scale was set individually for each snapshot using three-sigma rule, i.e., values diverging from the mean value more than three standard deviations were excluded from scaling. The maps are prepared for qualitative assessment, thus actual strain values are not presented (they will be discussed further).
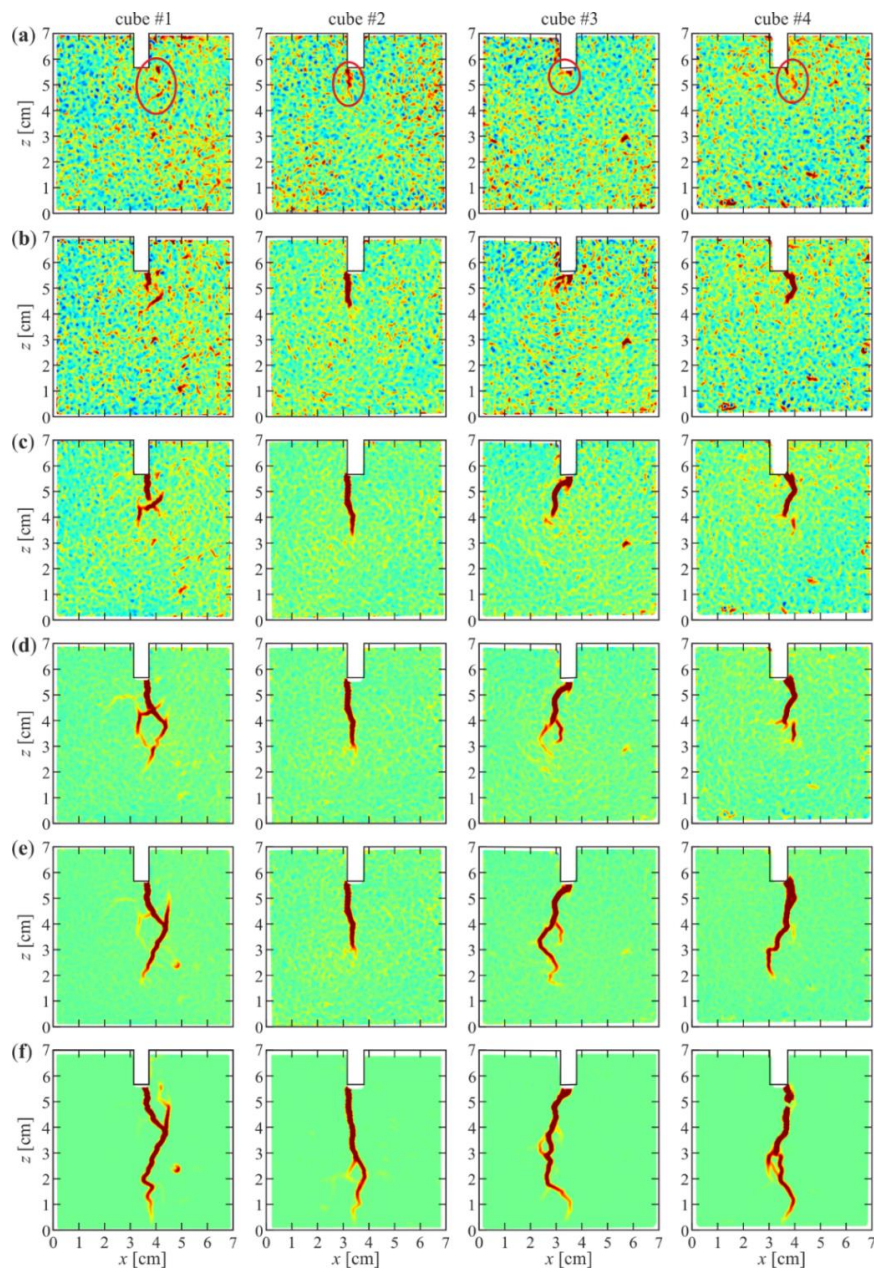

Figure 5. Snapshots of major strain ε_1 representing the evolution of FPZs for cubes #1 – #4 at different load levels in relation to maximum force: initiation of FPZs (**a**); 90% pre-peak (**b**); peak value (**c**); 90% post-peak (**d**); 70% post-peak (**e**); and end of the test (**f**)

By analysing the evolution of FPZs, it can be stated that the behaviour of all cubes was similar. The first set of snapshots (Figure 5a) shows the moment of clear initiation of FPZs (marked by red circles). FPZs appear at different relative load levels (48–73% of the maximum load) and times for different cubes, however, the corresponding CMOD values are close (see Table 1). The corresponding strain values are equal to about 1‰, which may indicate the initiation of micro-cracking, which, however, does not yet indicate the presence of visible cracks. For further time instances, the FPZs reach a similar depth and by the end of the test (Figure 5f), they cover almost the whole height of all cubes. Fracture process zones are noticeably curved and sometimes branching phenomena can be noticed (Figure 5a and 5c). Localised strain zones reached the bifurcation point at which the lowest energy path was followed. Curvature of FPZ zones is mainly determined by the heterogeneous structure of the elements, e.g., the presence of aggregate grains. The micro-cracking region changes its area during the deformation process since at the beginning micro-cracks arise until the moment where micro-cracking turns into final macro-crack and simultaneously number of micro-cracks start closing. Taking this fact into account, it is beneficial to analyse the strain and displacement values in the direction perpendicular to the expected crack (here, horizontal direction along the x axis). A single lateral cross-section below the notch tip (see Figure 1c) was assumed for the analysis of each cube.

Table 1. Corresponding characteristics (percentage of peak load, time, and CMOD) in the moment of FPZs initiation for cubes #1 – #4.

Cube	Time instance [s]	Percentage of F_{max} (pre-peak)	CMOD [mm]
#1	448	73%	0.0035
#2	412	48%	0.0036
#3	564	66%	0.0036
#4	470	69%	0.0041

Figure 6 shows the major strain (left column) and lateral translation (right column) along the specified lines. The values are presented for different instances based on the percentage of peak value: $0 – 90\% F_{max}$ pre-peak (blue line), F_{max} (green dashed line), and $90\% – 0\%$ F_{max} post-peak (red lines). Major strains, representing the localization of FPZs, are first discussed. It is important to note that in the area of crack formation, the presented strains are not actual strains in the material, they are artificially overestimated because the distance between two particular points on the analysed surface may be increased by the already appeared crack (there is no material to actually carry those strains). At the moment of maximum load, the strain reaches a level of 6 – 11‰ which is far above the limit strain for typical concretes, thus it is an obviously cracked state. Some cracks should have appeared during the pre-peak stage, which

13

also stays in agreement with the FPZs localised in DIC maps (Figure 5). During the post-peak behaviour, the strain values are further increasing and, by the end of the test, exceeds 230‰ (cubes #1 and #2) or reaches almost 120‰ (cube #3) and 150‰ (cube #4). The large (in fact, artificial) strain values allow stating about the advanced macro-cracking state. An important issue is the determination of the exact moment of macro-crack initiation, which is expected to occur after the peak load. At the moment of reaching a peak load, the strains were too low to unquestionably indicate the occurrence of macro-cracks. It has to be mentioned that the observation of strain values may not be effective for the determination of macro-crack initiation, thus a useful approach can be applied, based on the study of local lateral translation along the assumed cross-sections (Figure 6, right column). It can be observed that no significant displacement is observed during the pre-peak stage of loading. The translations seem to be uniform and relatively small, close to zero. While reaching a peak load, a discontinuity appears, where the value changes the sign. At this moment, the displacement does not exceed 0.01 mm in both (left and right) directions. After passing through the peak load, the divergence between both sides of the discontinuity (destined crack) increases, giving absolute extreme values between 0.1 and 0.2 mm.
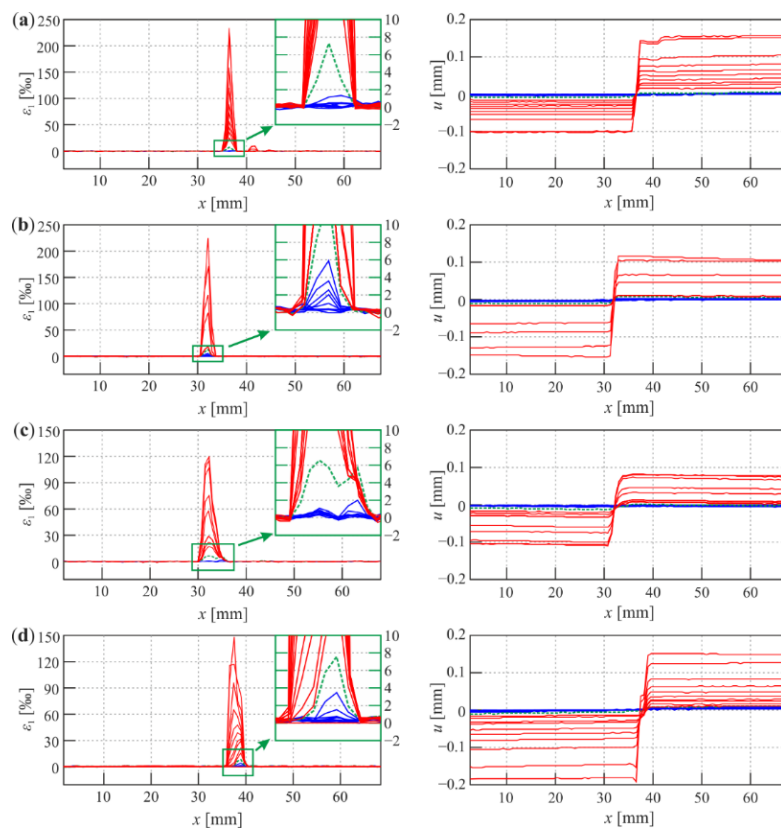

Figure 6. Major strain (left column) and lateral translation (right column) along the assumed cross-sections (in the x axis) for cubes #1 – #4 at different load levels in relation to the maximum force ($0 – 90\% F_{max}$ pre-peak – blue lines, peak – green dashed line, and $90 – 0\% F_{max}$ post-peak – red lines, global step of 10%): cube #1 (**a**); cube #2 (**b**); cube #3 (**c**); cube #4 (**d**)

14

The above-described changes in lateral translation can be further processed to obtain a moment of macro-crack initiation. For this purpose, the amplitude of displacements (difference between extreme values at a specific time instance) was calculated to be further considered as a crack width. Figure 7a presents the changes in the amplitude of lateral displacement over time, the moment of peak load is also marked. It is clear that before the peak load there are no significant changes in the amplitude. It is almost uniform and does not exceed 0.02 mm for all cubes. A slight increase can be observed near the peak value, which corresponds to the clear development of FPZs and, probably, advanced micro-cracking. A sharp increase can be observed after the peak load for all cubes, and then, a monotonic increase of amplitude occurs until the end of the test. These sudden leaps correspond to the macro-crack initiation, thus it is beneficial to determine the exact moment of their occurrence. In this case, a well-known tool, i.e., continuous wavelet transform (CWT) can be very useful. A Gaussian wavelet with one vanishing moment (gaus1) was chosen for calculation, based on its correspondence to the first derivative, representing rotation angles of the transformed function. A motivation for using CWT instead of the conventional derivative is its significant advantage of overcoming a measurement noise. Figure 7b shows the CWT scalogram prepared for scales between 1 and 20. For further consideration, a specific scale $s = 5$ was chosen (marked by a red dashed line). Particular wavelet transforms are presented in Figure 7c. The moment of macro-crack initiation is visible for each cube and can be located in time when CWT achieves a local maximum. The results for all cubes are presented in Table 2. It is clear that the obtained CMOD values (reflecting the crack width w) when the macro-crack occurred are significant. In the case of cubes #2 and #3, the value sharply changes to about 0.1 mm, which can be clearly interpreted as macro-crack. For cubes #1 and #4, the moment of macro-crack formation is not that sharp, thus CMODs are lower but still significant.
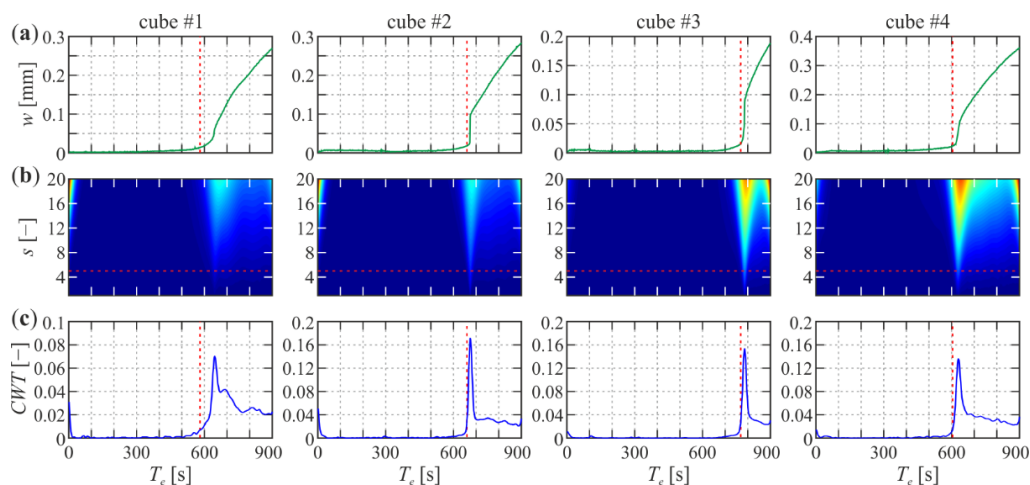

Figure 7. Determination of macro-crack occurrence for cubes #1 – #4: amplitude of horizontal translation along assumed cross-sections (**a**); scalogram of CWT (**b**); wavelet transform for scale $s = 5$ (**c**)

15

Table 2. Corresponding characteristics (time, percentage of peak load, and CMOD) in the moment of macro-crack initiation for cubes #1 – #4.

Cube	Time instance [s]	Percentage of F_{max} (post-peak)	CMOD [mm]
#1	646	71%	0.0672
#2	674	39%	0.1049
#3	786	43%	0.0997
#4	630	59%	0.0825

3.3. X-Ray Micro-Computed Tomography

X-ray micro-computed tomography scans after fracture present the changes of macro-crack path in the internal structure of each cube (Figure 8). The macro-cracks were identified in the prepared scans based on the visual assessment and drawn to obtain clear imaging. In the case of vertical cross-sections (Figure 9), the agreement with DIC results is clearly visible (cf. Figure 9a and Figure 5f). The shapes of the cracks are identical, which confirms the appropriateness of the prepared DIC visualisations. The crack paths are concentrated in the central part of the scans, which results from the applied splitting load, and is clearly visible for all cross-sections. The cracks mainly avoid aggregates, especially with greater sizes (mostly visible in Figure 9a, cube #3 and #4, Figure 9c, cube #1, or Figure 9a, cube #1). However, while the aggregate is located near the notch tip, the crack breaks it, e.g., cube #2, Figure 9a,e. The cracks cover almost the whole height of all samples what also stays in agreement with DIC visualization.
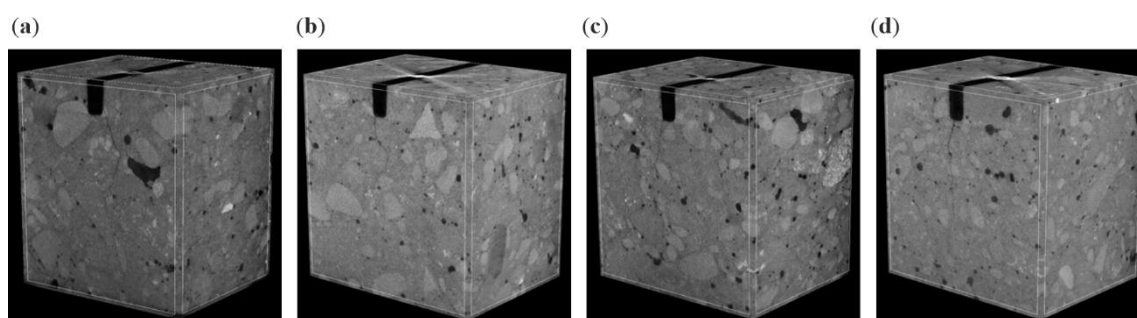

Figure 8. 3D X-ray micro-CT images of cracked cubic specimens at depth y = 17.5 mm after failure: cube #1 (**a**); cube #2 (**b**); cube #3 (**c**); and cube #4 (**d**)
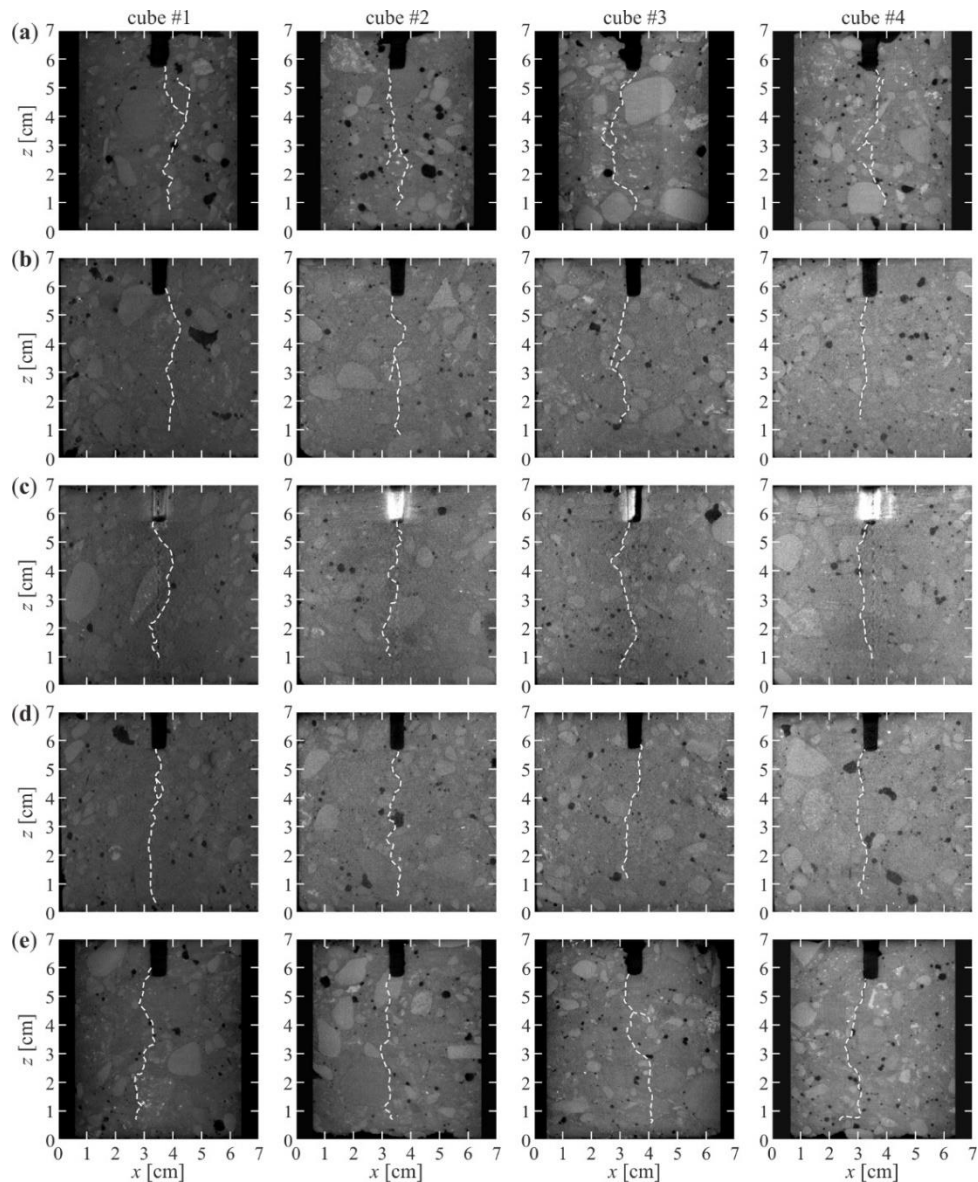
16

Figure 9. Micro-CT images of cubes #1 – #4 (crack paths marked in white dashed lines) for vertical cross-sections located at different depths: $y = 0$ mm – front face (**a**); $y = 17.5$ mm (**b**); $y = 35$ mm (**c**); $y = 52.5$ mm (**d**); $y = 70$ mm – rear face (**e**)

3.4. CWI for damage monitoring

3.4.1. Coda wave detection

It is firstly important to note that determination of the exact time range of coda wave presence is not a trivial issue. In the current paper, a simple algorithm for coda wave searching is proposed. Firstly, the signal is divided into a number of small parts, using a constant time step (time window). Secondly, the decorrelation coefficient is calculated individually for each of those parts using Eq. (1), for the assumed set of signals. Then, the 3D surface can be plotted, representing DC values in relation to the start point of each consecutive part and the time of degradation. This visualization is expected to give information about the appropriate coda wave range by observing the intensification of DC. For the analysed samples, the calculations were

17

conducted for the time range of 0 – 1 ms with four lengths of time window dt, i.e., 0.02 ms, 0.05 ms, 0.1 ms, and 0.2 ms. Figure 10 shows the results of coda wave searching for cube #1, based on both sensors S1 and S2. It is noteworthy that the length of the time window does not change the images in general. Larger values of dt result in smoother maps, but, on the other hand, cause a loss of the map resolution. As a compromise, the length of 0.05 ms was chosen for further analyses. Maps for sensor S1 (Figure 10a) clearly detects coda waves; a significant increase is observed in the signal time range of about 0.10 – 0.25 ms, regardless of the length of the time window. For the time lower than 0.10 ms (direct waves) and above 0.25 ms (noisy range), the DC values are significantly lower. The DC values are also low for an initial time of the test (before 400 s), regardless of the signal time, because no significant changes are observed in the analysed specimens (this will be further discussed). In the case of sensor S2 (Figure 10b), the presence of coda waves is also visible. However, the high DC values are also visible in a noisy range throughout the whole test. The noise in sensor S2 has a complex character, which could be the effect of a significant distance between the actuator and S2. To sum up, the clear coda wave detection was provided by the sensor located near the actuator (S1) and the assumed range is 0.10 – 0.25 ms. Concerning the time of flight through the specimen (0.0148 ms), the wave was capable of multiple propagation (approximately 10) through the sample in the established time range. Assuming that the scattering mean free path is of order of 15 mm, the scattering mean free time equals 0.0032 ms, resulting with about 4.6 scattering events at a single flight through the probed volume (about 47 events in the assumed coda wave range). The assumed range was then verified for other samples. Figure 11 shows the DC maps for all cubes for the chosen $dt = 0.05$ ms altogether with the assumed range marked. It is clear that the established range is suitable for all cubes for sensor S1. In the case of sensor S2, the range is not as fitted, because the signals are much more disrupted due to the significant distance from the actuator. It is important to note that the intensification of DC occurs before reaching the peak load, which creates the possibility of early damage detection.
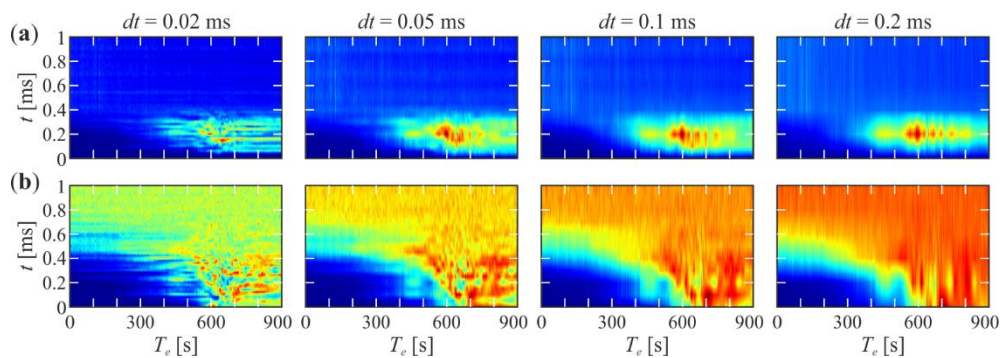

Figure 10. Detection of time range of coda wave presence for cube #1 for different lengths of time window at sensors S1 (**a**) and S2 (**b**)
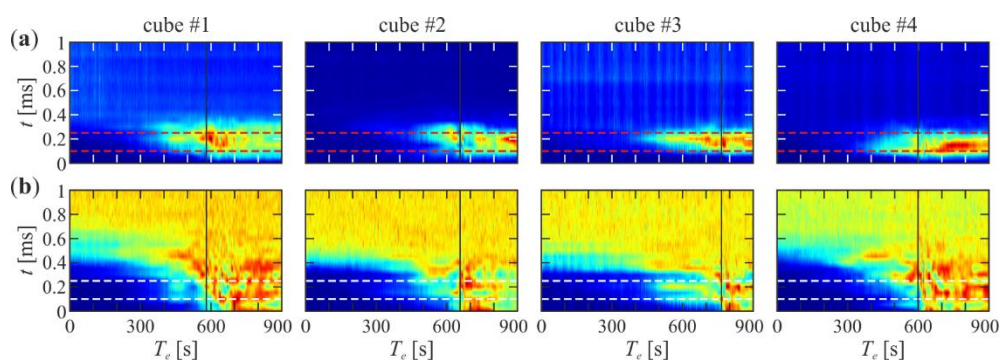
18

Figure 11. Verification of the assumed time range of coda wave (dashed lines) for cubes #1 – #4 for a time window length of 0.05 ms (moment of maximum force marked with solid lines) at sensors S1 (**a**) and S2 (**b**)

3.4.2. *Decorrelation of time-domain signals*

Having determined the appropriate time range for coda waves, the calculation of DC for each time instance was performed. Figure 12 shows the changes of DC during the split tests. Specific time instances are additionally marked by vertical dashed lines: the first appearance of FPZs on the sample surface (red), peak load (orange), and macro-crack initiation (green). Based on the characteristics of the DC functions and those instances, some stages can be characterized during the performed tests. It is important to establish some thresholds for DC values. The first limit can be determined at the level of $L_I = 0.1$, determining stage 1 of tests (for both sensors). Since the moment of reaching this value, DC grows monotonically and this increase is relatively slow and stable which could result from subtle changes in the stress state. No significant changes in the sample structure occur, thus this stage can be called as an intact state. After reaching L_I, stage 2 occurs, in which DC increases more rapidly (observed more evidently for cubes #1 and #4 by the change in curve direction). During this step, the initiation and coalescence of micro-cracks occur. Some randomly localised micro-cracks appear in the structure of the sample and, due to load increase, the micro-cracks merge to initiate FPZs, thus DIC images should indicate on FPZs formation. However, it has to be noted that the initiation of FPZs (red lines in the charts) was determined for a single sample surface (the photographed one) so it may not be entirely reliable, because, micro-cracking could initiate earlier inside the specimen or at the opposite surface what could not be observed in DIC maps. Nevertheless, it is noteworthy that the determination of L_I is actually not a crucial issue because the presence of micro-cracks is a normal phenomenon in concrete structures. Simultaneously, the appearance of FPZ may indicate future crack formation, thus the limit between stages 2 and 3 (L_{II}) is more important. It can be established as $L_{II} = 0.4$ for both sensors. After reaching this level, some significant disturbances can be observed in the curves, however, the values still increase, in general. Stage 3 is characterized by stable micro-crack propagation after the initiation of FPZs. The micro-cracks are already visible in DIC images at the surface of the cubes (the red lines

19

indicating FPZs appearance were observed in the previous stage 2). The moment of reaching the peak load is present in stage 3 for most cubes (see orange line). Local minimum of DC function can be observed at this moment for sensor S1, on the other hand, local maximum occurs for sensor S2 (cube #4 is the exception because the local maximum is for sensor S2). Stage 3 ends with a sharp increase in DC values, reaching the third limit, equal to $L_{III} = 0.7$ for sensor S1 and $L_{III} = 1.0$ for sensor S2 which corresponds to the appearance of macro-crack. This starts stage 4 where the already formed macro-crack propagates uncontrollably, indicating severe sample damage. The behaviour of DC is highly disordered due to the significant sample fracture which influences the wave signals. The values increase and decrease, however, they do not decrease below 0.5 (sensor S1) and 0.8 (S2).
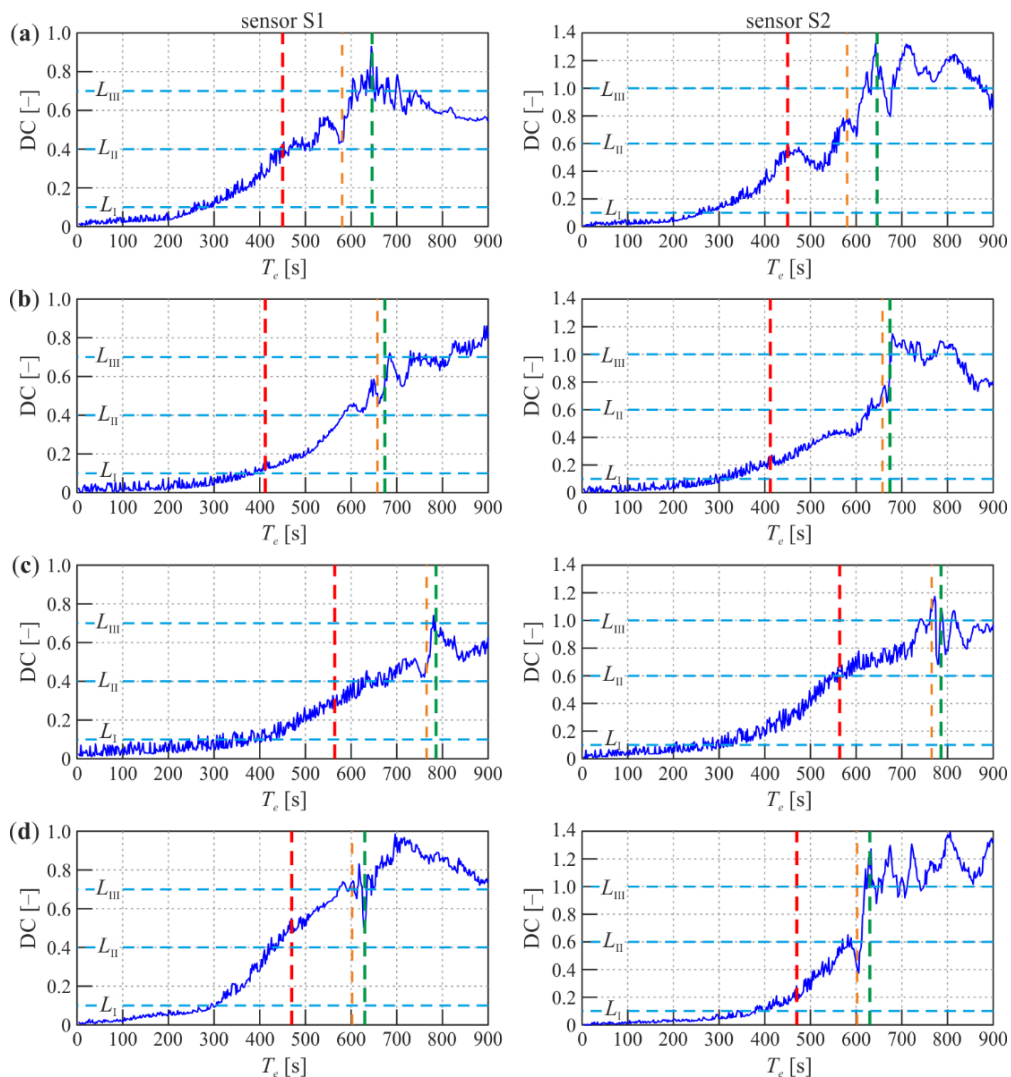

Figure 12. DC of coda waves in the assumed range of 0.1 – 0.25 ms for sensors S1 (left column) and S2 (right column): cube #1 (**a**); cube #2 (**b**); cube #3 (**c**); cube #4 (**d**)

To sum up, in the case of potential applications for non-destructive damage detection without a visual assessment of the analysed specimens, we can consider two scenarios. Firstly, in situ monitoring, where a complete history of loading for an analysed object is known, when

20

the serious damage state can be determined after reaching $L_{II} = 0.7$ for the sensor placed near the actuator and $L_{II} = 1.0$ for the sensors placed opposite to the expected crack. Secondly, while having only a reference measurement and another one in the actual state, the risk of underestimating the DC in stage 4 occurs. For this reason, more restricted limits need to be established, and it can be said that the inacceptable DC values are above 0.5 and 0.8 (minima in stage 4) for the two sensors, close and far from the actuator, respectively.

3.4.3. Decorrelation of frequency spectra

As an additional part of the analysis, FFT was calculated for signals in the determined coda wave range. Figure 13 presents the transforms of all signals collected during tests set together as a 2D surface. Some significant disturbances (differences in amplitudes) can be observed in the frequency spectra for all cubes (at both sensors), especially after reaching the peak load. This fact allows stating that the decorrelation of FFT of coda waves can be also useful in non-destructive damage detection. DC was then calculated using Eq. (3) in a frequency range of 400 – 600 kHz, where significantly non-zero values were observed in FFTs (range marked in the charts).
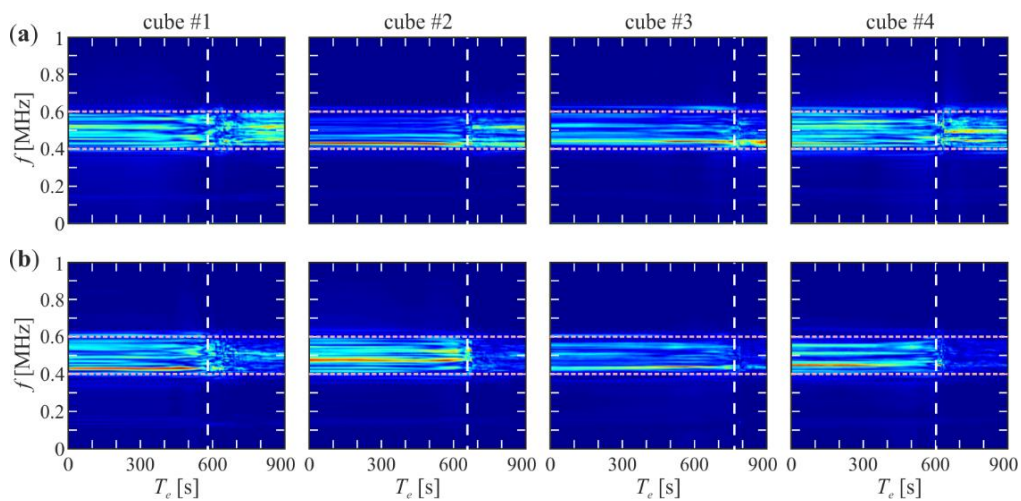

Figure 13. FFT of coda waves in the assumed range of 0.1 – 0.25 ms for cubes #1 – #4 (moment of maximum load value marked with white dashed lines) at sensors S1 (**a**) and S2 (**b**)
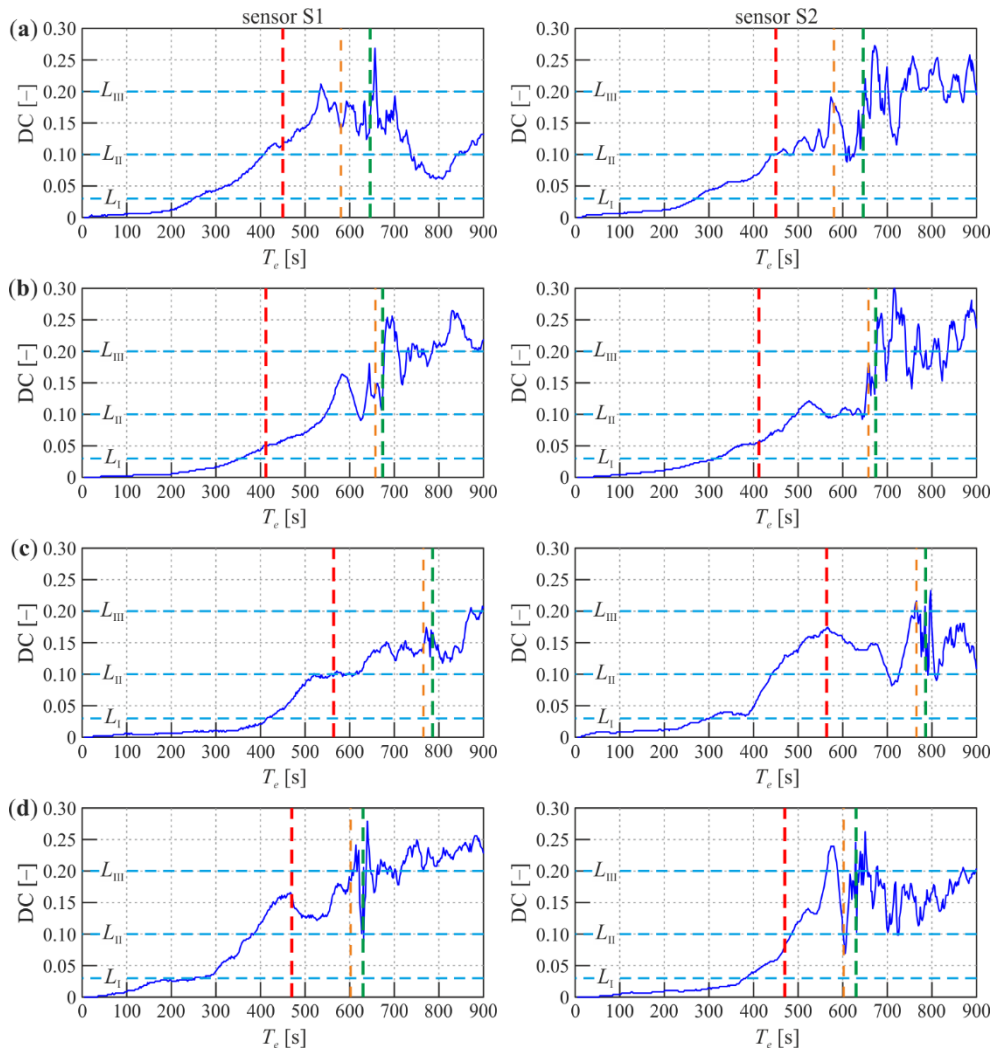
Figure 14. DC of FFT of coda waves in the assumed frequency range of 400 – 600 kHz for sensors S1 (left column) and S2 (right column): cube #1 (**a**); cube #2 (**b**); cube #3 (**c**); cube #4 (**d**)

Figure 14 shows the changes of DC calculated from the frequency spectra of the following ultrasonic wave signals. The resemblance to the previously discussed Figure 12 is evident. The analogical fracture stages can be established based on the DC level, however, the functions are free of noise and the values are significantly lower. The first stage (intact state) can be determined below the limit $L_I = 0.03$ for both sensors. DC increases significantly above this limit for all concrete cubes. Next, stage 2 occurs (micro-crack initiation and coalescence), where FPZs at the DIC analysed side are present for cubes #2 and #3. For cubes #1 and #4, FPZs appear later, however, it is probable that they initiate earlier aside from this surface. Stage 2 finishes with the second limit $L_{II} = 0.1$, for which stage 3 initiates with stable micro-crack propagation. During this step, some significant disturbances can be observed in DC functions. Like for DC calculated for time-domain signals, local minima are observed in the moment of peak load for sensor S1 and local maxima for sensor S2 (also, sensor S2 for cube #4 is the exception to this rule). Stage 3 ends with macro-crack appearance which occurs at the third DC

22

limit equal to approximately $L_{III} = 0.2$ for both sensors. It is important to note that this limit is constant, but it was previously differentiated between sensors. This fact could be treated as a significant advantage of analysing DC in the frequency spectra because it seems that the location of the sensor is not crucial in this case. However, some exceptions need to be noted. Firstly, for some functions (cube #1, sensor S1 and cube #4, sensor S2), the established limit L_{III} is reached before the macro-crack initiation. For those examples, the limit could be estimated as 0.22 and 0.24, respectively. However, it is noteworthy that the increase of this limit can signalise the damage state before it actually occurs, thus it can only be a more strict (safer) assessment. What is more, for cube #3 at sensor S2 value should be lowered to 0.17 which could result in underestimating the damage state. However, this difficulty can be easily overcome in practice by analysing the signals from more than one sensor and taking as reliable the one with the most strict assessment (in this case, sensor S1 gave an appropriate establishment of macro-crack initiation).

To sum up, analysing the DC of frequency spectra gives similar information about the damage state as DC of time-domain signals, however, it has some significant advantages. Firstly, the DC functions are smoother, they do not have a noisy character which allows a more accurate approximation of DC value. Secondly, the DC values are close for the sensors placed in significantly different locations which allows using equal DC limits.

4. Conclusions

The paper dealt with the continuous-time monitoring of mechanical degradation in concrete cubes under splitting. The fracture process was characterized by the integrated DIC and CWI techniques, supported by micro-CT scanning. A series of original experiments was performed to determine the applicability of the proposed techniques in early damage detection and their limitations.

As a well-known and highly developed technique, DIC was successfully used to visualize the crack evolution for all cubes in detail. The mechanical behaviour of all tested beams was similar. DIC allowed detecting the moment of fracture process zone appearance and micro-crack initiation. However, it gave information about the actual state of the specimen only at a single surface without giving any information about the state of the sample internal structure. Observation of local major strains and translations in a specific cross-section was used to determine the moment of macro-crack initiation. Significant support of CWT was appreciated in this case. Micro-CT allowed observation of the crack path inside the specimen in the final

23

state (after fracture). It also confirmed the appropriateness of the performed DIC calculations based on the resemblance of crack shape from both methods.

CWI technique was proved to be effective in the non-destructive assessment of damage level, thanks to the synchronized collection of DIC photographs and ultrasonic signals during fracture. It provided important information about fracture initiation before any fracture process zone was observed in DIC images. A simple approach to determine the appropriate coda wave range was proposed. DC functions were calculated for the time domain signals in the assumed coda wave range and their frequency spectra. Both approaches allowed the establishment of specific DC levels which determine the limits between four stages of fracture (intact state, micro-crack initiation and coalescence, stable micro-crack propagation, and macro-crack propagation). Based on the comparison of those approaches, decorrelation in the frequency domain turned out to have significant advantages, i.e., DC functions were noise-free and DC values were similar for sensors placed in different locations. It was revealed that the change of DC of coda waves could be applied in real-time monitoring of concrete fracture as an autonomous damage indicator.

Summarizing, the simultaneous application of DIC, CWI, and micro-CT techniques is effective in non-destructive damage detection of concrete cubes under splitting. The proposed framework has the potential to be used for monitoring of fracture process in other concrete elements. Future work will focus on applying the proposed approach for different types of specimens subjected to various loads, e.g., beams under bending tests. The influence of environmental factors, like temperature or humidity will be also studied. The limitations (e.g., the limit size of sample tested) and possibilities (the ability to estimate damage size and localization) of the proposed method are very important aspects for further considerations. The DC changes are desired to be attributed to the stress state in the material in different types of tests, e.g., compression or bending. What is more, the influence of relative velocity changes corresponding to the stresses will be also analysed. The current research can be also significantly developed by introducing micro-CT scanning during characteristic moments of the test. Additionally, micro-CT scans provide information about the sample microstructure that can be further used in numerical simulations of ultrasonic wave propagation.

Declaration of Competing Interest

The authors declare that they have no known competing financial interests or personal relationships that could have appeared to influence the work reported in this paper.

CRediT authorship contribution statement

Erwin Wojtczak: Conceptualization, Methodology, Software, Formal analysis, Visualisation, Writing - Original Draft. **Magdalena Rucka**: Conceptualization, Methodology, Experimental Investigation, Writing - Review & Editing, Supervision, Project administration, Funding acquisition. **Łukasz Skarżyński**: Experimental Investigation, Writing - Review & Editing.

References

[1] Ponikiewski T, Gołaszewski J, Rudzki M, Bugdol M. Determination of steel fibres distribution in self-compacting concrete beams using X-ray computed tomography. Arch Civ Mech Eng 2015;15:558–68. https://doi.org/10.1016/j.acme.2014.08.008.

[2] Ponikiewski T, Katzer J, Bugdol M, Rudzki M. X-ray computed tomography harnessed to determine 3D spacing of steel fibres in self compacting concrete (SCC) slabs. Constr Build Mater 2015;74:102–8. https://doi.org/10.1016/j.conbuildmat.2014.10.024.

[3] Loeffler CM, Qiu Y, Martin B, Heard W, Williams B, Nie X. Detection and segmentation of mechanical damage in concrete with X-Ray microtomography. Mater Charact 2018;142:515–22. https://doi.org/10.1016/j.matchar.2018.06.018.

[4] Vicente MA, Mínguez J, González DC. Computed tomography scanning of the internal microstructure, crack mechanisms, and structural behavior of fiber-reinforced concrete under static and cyclic bending tests. Int J Fatigue 2019;121:9–19. https://doi.org/10.1016/j.ijfatigue.2018.11.023.

[5] Skarżyński Ł, Tejchman J. Investigations on fracture in reinforced concrete beams in 3-point bending using continuous micro-CT scanning. Constr Build Mater 2021;284. https://doi.org/10.1016/j.conbuildmat.2021.122796.

[6] Fayyad TM, Lees JM. Application of Digital Image Correlation to Reinforced Concrete Fracture. Procedia Mater Sci 2014;3:1585–90. https://doi.org/10.1016/j.mspro.2014.06.256.

[7] Gencturk B, Hossain K, Kapadia A, Labib E, Mo YL. Use of digital image correlation technique in full-scale testing of prestressed concrete structures. Meas J Int Meas Confed 2014;47:505–15. https://doi.org/10.1016/j.measurement.2013.09.018.

[8] Hamrat M, Boulekbache B, Chemrouk M, Amziane S. Flexural cracking behavior of normal strength, high strength and high strength fiber concrete beams, using Digital Image Correlation technique. Constr Build Mater 2016;106:678–92. https://doi.org/10.1016/j.conbuildmat.2015.12.166.

[9] Słoński M, Tekieli M. 2D digital image correlation and region-based convolutional neural network in monitoring and evaluation of surface cracks in concrete structural elements. Materials (Basel) 2020;13:3527. https://doi.org/10.3390/MA13163527.

[10] Li D, Huang P, Chen Z, Yao G, Guo X, Zheng X, et al. Experimental study on fracture and fatigue crack propagation processes in concrete based on DIC technology. Eng Fract Mech 2020;235:107166. https://doi.org/10.1016/j.engfracmech.2020.107166.

[11]   Miura T, Sato K, Nakamura H. The role of microcracking on the compressive strength and stiffness of cracked concrete with different crack widths and angles evaluated by DIC. Cem Concr Compos 2020;114:103768. https://doi.org/10.1016/j.cemconcomp.2020.103768.

[12]   Suchorzewski J, Prieto M, Mueller U. An experimental study of self-sensing concrete enhanced with multi-wall carbon nanotubes in wedge splitting test and DIC. Constr Build Mater 2020;262:120871. https://doi.org/10.1016/j.conbuildmat.2020.120871.

[13]   Iturrioz I, Lacidogna G, Carpinteri A. Acoustic emission detection in concrete specimens: Experimental analysis and lattice model simulations. Int J Damage Mech 2014;23:327–58. https://doi.org/10.1177/1056789513494232.

[14]   Verbruggen S, De Sutter S, Iliopoulos S, Aggelis DG, Tysmans T. Experimental Structural Analysis of Hybrid Composite-Concrete Beams by Digital Image Correlation (DIC) and Acoustic Emission (AE). J Nondestruct Eval 2016;35:1–10. https://doi.org/10.1007/s10921-015-0321-9.

[15]   Logoń D, Schabowicz K. The recognition of the micro-events in cement composites and the identification of the destruction process using acoustic emission and sound spectrum. Materials (Basel) 2020;13:2988. https://doi.org/10.3390/ma13132988.

[16]   Chakraborty J, Katunin A, Klikowicz P, Salamak M. Early crack detection of reinforced concrete structure using embedded sensors. Sensors (Switzerland) 2019;19:1–22. https://doi.org/10.3390/s19183879.

[17]   Deraemaeker A, Dumoulin C. Embedding ultrasonic transducers in concrete: A lifelong monitoring technology. Constr Build Mater 2019;194:42–50. https://doi.org/10.1016/j.conbuildmat.2018.11.013.

[18]   Rucka M. Failure Monitoring and Condition Assessment of Steel-Concrete Adhesive Connection Using Ultrasonic Waves. Appl Sci 2018;8:320. https://doi.org/10.3390/app8030320.

[19]   Lin S, Shams S, Choi H, Azari H. Ultrasonic imaging of multi-layer concrete structures. NDT E Int 2018;98:101–9. https://doi.org/10.1016/j.ndteint.2018.04.012.

[20]   Zamen S, Dehghan-Niri E. Fractal analysis of nonlinear ultrasonic waves in phase-space domain as a quantitative method for damage assessment of concrete structures. NDT E Int 2020;111:102235. https://doi.org/10.1016/j.ndteint.2020.102235.

[21]   Aki K, Chouet B. Origin of coda waves: Source, attenuation, and scattering effects. J Geophys Res 1975;80:3322–42. https://doi.org/10.1029/JB080i023p03322.

[22]   Planès T, Larose E. A review of ultrasonic Coda Wave Interferometry in concrete. Cem Concr Res 2013;53:248–55. https://doi.org/10.1016/j.cemconres.2013.07.009.

[23]   Spytek J, Pieczonka L, Stepinski T, Ambrozinski L. Mean local frequency-wavenumber estimation through synthetic time-reversal of diffuse Lamb waves. Mech Syst Signal Process 2021;156:107712. https://doi.org/10.1016/j.ymssp.2021.107712.

[24]   Larose E, De Rosny J, Margerin L, Anache D, Gouedard P, Campillo M, et al. Observation of multiple scattering of kHz vibrations in a concrete structure and application to monitoring weak changes. Phys Rev E - Stat Nonlinear, Soft Matter Phys 2006;73. https://doi.org/10.1103/PhysRevE.73.016609.

[25]   Wunderlich C, Niederleithinger E. Evaluation of temperature influence on ultrasound velocity in concrete by coda wave interferometry. Int. Symp. Nondestruct. Test. Mater. Struct., Springer; 2011, p. 227–32. https://doi.org/10.1007/978-94-007-0723-8_33.

[26] Zhang Y, Abraham O, Tournat V, Le Duff A, Lascoup B, Loukili A, et al. Validation of a thermal bias control technique for Coda Wave Interferometry (CWI). Ultrasonics 2013;53:658–64. https://doi.org/10.1016/j.ultras.2012.08.003.

[27] Stähler SC, Sens-Schönfelder C, Niederleithinger E. Monitoring stress changes in a concrete bridge with coda wave interferometry. J Acoust Soc Am 2011;129:1945–52. https://doi.org/10.1121/1.3553226.

[28] Zhang Y, Abraham O, Duff A Le, Lascoup B, Tournat V, Larose E, et al. Monitoring the Stress Level of Concrete Structures with CODA Wave Interferometry: Experimental Illustration of an Investigated Zone. Int. Symp. Nondestruct. Test. Mater. Struct., Springer; 2011, p. 233–8. https://doi.org/10.1007/978-94-007-0723-8_34.

[29] Chen B, Callens D, Campistron P, Moulin E, Debreyne P, Delaplace G. Monitoring cleaning cycles of fouled ducts using ultrasonic coda wave interferometry (CWI). Ultrasonics 2019;96:253–60. https://doi.org/10.1016/j.ultras.2018.12.011.

[30] Sang G, Liu S, Elsworth D. Quantifying fatigue-damage and failure-precursors using ultrasonic coda wave interferometry. Int J Rock Mech Min Sci 2020;131:104366. https://doi.org/10.1016/j.ijrmms.2020.104366.

[31] Hafidi Alaoui H, Rodriguez S, Deschamps M. Detection of defects in a 2D fluid-solid periodic cluster. Ultrasonics 2021;112:106307. https://doi.org/10.1016/j.ultras.2020.106307.

[32] Pomarède P, Chehami L, Declercq NF, Meraghni F, Dong J, Locquet A, et al. Application of Ultrasonic Coda Wave Interferometry for Micro-cracks Monitoring in Woven Fabric Composites. J Nondestruct Eval 2019;38:1–8. https://doi.org/10.1007/s10921-019-0563-z.

[33] Zhu Q, Yu K, Li H, Zhang H, Ding Y, Tu D. A loading assisted diffuse wave inspection of delamination in a unidirectional composite. Appl Acoust 2021;177:107868. https://doi.org/10.1016/j.apacoust.2020.107868.

[34] Gao F, Wang L, Hua J, Lin J, Mal A. Application of Lamb wave and its coda waves to disbond detection in an aeronautical honeycomb composite sandwich. Mech Syst Signal Process 2021;146:107063. https://doi.org/10.1016/j.ymssp.2020.107063.

[35] Schurr DP, Kim JY, Sabra KG, Jacobs LJ. Damage detection in concrete using coda wave interferometry. NDT E Int 2011;44:728–35. https://doi.org/10.1016/j.ndteint.2011.07.009.

[36] Schurr DP, Kim JY, Sabra KG, Jacobs LJ. Monitoring damage in concrete using diffuse ultrasonic coda wave interferometry. AIP Conf Proc 2011;1335:1283–90. https://doi.org/10.1063/1.3592081.

[37] Shokouhi P. Stress- and damage-induced changes in coda wave velocities in concrete. AIP Conf Proc 2013;1511:382–9. https://doi.org/10.1063/1.4789073.

[38] Planès T, Larose E, Margerin L, Rossetto V, Sens-Schönfelder C. Decorrelation and phase-shift of coda waves induced by local changes: Multiple scattering approach and numerical validation. Waves in Random and Complex Media 2014;24:99–125. https://doi.org/10.1080/17455030.2014.880821.

[39] Planès T, Larose E, Rossetto V, Margerin L. Imaging multiple local changes in heterogeneous media with diffuse waves. J Acoust Soc Am 2015;137:660–7. https://doi.org/10.1121/1.4906824.

[40] Hilloulin B, Zhang Y, Abraham O, Loukili A, Grondin F, Durand O, et al. Small crack detection in cementitious materials using nonlinear coda wave modulation. NDT E Int 2014;68:98–104. https://doi.org/10.1016/j.ndteint.2014.08.010.

[41] Liu S, Zhu J, Wu Z. Implementation of Coda Wave Interferometry Using Taylor Series Expansion. J Nondestruct Eval 2015;34:1–6. https://doi.org/10.1007/s10921-015-0300-1.

[42] Larose E, Obermann A, Digulescu A, Planès T, Chaix J-F, Mazerolle F, et al. Locating and characterizing a crack in concrete with diffuse ultrasound: A four-point bending test. J Acoust Soc Am 2015;138:232–41. https://doi.org/10.1121/1.4922330.

[43] Zhang Y, Larose E, Moreau L, d'Ozouville G. Three-dimensional in-situ imaging of cracks in concrete using diffuse ultrasound. Struct Heal Monit 2018;17:279–84. https://doi.org/10.1177/1475921717690938.

[44] Fröjd P, Ulriksen P. Frequency selection for coda wave interferometry in concrete structures. Ultrasonics 2017;80:1–8. https://doi.org/10.1016/j.ultras.2017.04.012.

[45] Xie F, Larose E, Moreau L, Zhang Y, Planes T. Characterizing extended changes in multiple scattering media using coda wave decorrelation: numerical simulations. Waves in Random and Complex Media 2018;28:1–14. https://doi.org/10.1080/17455030.2017.1308042.

[46] Hafiz A, Schumacher T. Monitoring of Stresses in Concrete Using Ultrasonic Coda Wave Comparison Technique. J Nondestruct Eval 2018;37:1–13. https://doi.org/10.1007/s10921-018-0527-8.

[47] Spalvier A, Cetrangolo G, Martinho L, Kubrusly A, Blasina F, Perez N. Monitoring of compressive stress changes in concrete pillars using cross correlation. IEEE Int Ultrason Symp IUS 2019;2019-October:2465–8. https://doi.org/10.1109/ULTSYM.2019.8926154.

[48] Hu H, Li D, Wang L, Chen R, Xu X. An improved ultrasonic coda wave method for concrete behavior monitoring under various loading conditions. Ultrasonics 2021; 116:106498. https://doi.org/10.1016/j.ultras.2021.106498.

[49] Rouchier S, Foray G, Godin N, Woloszyn M, Roux JJ. Damage monitoring in fibre reinforced mortar by combined digital image correlation and acoustic emission. Constr Build Mater 2013;38:371–80. https://doi.org/10.1016/j.conbuildmat.2012.07.106.

[50] Zhang F, Garnica GIZ, Yang Y, Lantsoght E, Sliedrecht H. Monitoring shear behavior of prestressed concrete bridge girders using acoustic emission and digital image correlation. Sensors (Switzerland) 2020;20:1–21. https://doi.org/10.3390/s20195622.

[51] Skarżyński Ł. Mechanical and radiation shielding properties of concrete reinforced with boron-basalt fibers using Digital Image Correlation and X-ray micro-computed tomography. Constr Build Mater 2020;255. https://doi.org/10.1016/j.conbuildmat.2020.119252.

[52] Skarżyński Ł, Marzec I. Shear fracture of longitudinally reinforced concrete beams under bending using Digital Image Correlation and FE simulations with concrete micro-structure based on X-ray micro-computed tomography images. Constr Build Mater 2021;274. https://doi.org/10.1016/j.conbuildmat.2020.122116.

[53] Rucka M, Wojtczak E, Knak M, Kurpińska M. Characterization of fracture process in polyolefin fibre-reinforced concrete using ultrasonic waves and digital image correlation. Constr Build Mater 2021;280. https://doi.org/10.1016/j.conbuildmat.2021.122522.

[54] Rucka M, Skarżyński Ł, Wojtczak E. Ultrasonic wave propagation, digital image correlation and X-ray micro-computed tomography measurements of concrete during splitting (cube #1) [Data set]. Gdańsk University of Technology 2021. https://doi.org/10.34808/8rw8-tj96

[55] Rucka M, Skarżyński Ł, Wojtczak E. Ultrasonic wave propagation, digital image correlation and X-ray micro-computed tomography measurements of concrete during splitting (cube #2) [Data set]. Gdańsk University of Technology 2021. https://doi.org/10.34808/04mv-e820

[56] Rucka M, Skarżyński Ł, Wojtczak E. Ultrasonic wave propagation, digital image correlation and X-ray micro-computed tomography measurements of concrete during splitting (cube #3) [Data set]. Gdańsk University of Technology 2021. https://doi.org/10.34808/9g3e-r789

[57] Rucka M, Skarżyński Ł, Wojtczak E. Ultrasonic wave propagation, digital image correlation and X-ray micro-computed tomography measurements of concrete during splitting (cube #4) [Data set]. Gdańsk University of Technology 2021. https://doi.org/10.34808/7jdh-wv39